Estuarine, Coastal and Shelf Science 278 (2022) 108091

Contents lists available at ScienceDirect

Estuarine, Coastal and Shelf Science

journal homepage: www.elsevier.com/locate/ecss

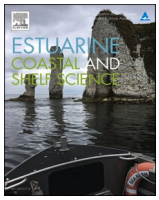

Impacts of high-resolution atmospheric forcing and air-sea coupling on coastal ocean circulation off the Pearl River Estuary

Wenfeng Lai [a,b], Jianping Gan [a,b,*]

[a] Department of Ocean Science, The Hong Kong University of Science and Technology & Southern Marine Science and Engineering Guangdong Laboratory, Zhuhai, China
[b] Department of Mathematics, The Hong Kong University of Science and Technology & Southern Marine Science and Engineering Guangdong Laboratory, Zhuhai, China

ARTICLE INFO

Keywords:
Estuarine-coastal circulation
Coupled air-sea modeling
Coastal circulation and transport

ABSTRACT

We investigated the impacts of high-resolution atmospheric forcing and ocean-atmosphere coupling on the estuary-shelf ocean simulation off the Pearl River Estuary. We conducted process and dynamics analyses of the wind-driven coastal ocean circulation under atmospheric flux forcing from (1) global reanalysis data, (2) a high-resolution regional atmospheric model, and (3) an air-sea coupled model during an upwelling-favorable wind. The results revealed that the high-resolution atmospheric model significantly improved the representations of the near-surface wind field and air temperature. The air-sea coupled model outperformed the uncoupled model in simulating coastal currents, water temperature, and salinity. The high-resolution uncoupled model strengthened the surface wind stress and along-isobath pressure gradient force (PGF), resulting in an intensified cross-isobath transport. The improved wind forcing from the air-sea coupled model modulated the spatial variation of the net stress curl and vorticity advection and enhanced the along-isobath PGF for a stronger cross-isobath transport. The lower sea surface temperature (SST) in the air-sea coupled model reduced the air temperature and wind stress. Adjusting the SST in the air-sea coupled model improved the momentum fluxes and the associated ocean transport dynamics.

1. Introduction

Simulating coastal oceanic circulation is challenging because of multiple influences on the circulation like wind, tide, river discharge, and air-sea exchange. In particular, wind-driven ocean circulation determines the coastal circulation dynamics. When numerically simulating the ocean, the most common way to atmospherically force the coastal ocean is to interpolate the wind forcing from large-scale reanalysis data (e.g. ERA-40) (Myksvoll et al., 2011), using a few observation points within the study area (Zu and Gan, 2015) or using idealized wind data (Xie and Eggleston, 1999). Neither method reflects or resolves the complex regional scale of the atmospheric fluxes caused by local topographic features and land-air-sea interactions in the near-shore coastal water. To obtain high-resolution wind forcing for a coastal ocean model, dynamically downscaling atmospheric analysis data to a higher resolution is a more optimal method. An ocean model is driven by atmospheric fluxes related to spatially and temporally variable atmospheric variables from the atmosphere model. In addition, interaction and feedback between the atmosphere and the ocean at various temporal and spatial scales influence the oceanic and atmospheric circulations when the atmospheric and oceanic models are coupled. In an estuary-shelf coupled coastal system, the interactions are even more complex. The interactions among land, air, and sea involve dynamic and thermodynamic environments in the atmospheric and oceanic processes and the coupling of the three systems.

For our study, we used the Pearl River Estuary (PRE) as an example of an estuary-shelf system that we simulated with a regional ocean model. The PRE is a semi-enclosed coastal embayment in the northern South China Sea (NSCS, Fig. 1). The PRE is shaped like a trumpet and is 5 km wide at the northern end and 35 km wide at the southern end. Two longitudinally deep channels vary from 5 m to 25 m in the central region and on the east side. These two deep channels connect the PRE with the adjacent NSCS. The water depth over the NSCS increases from 5 m at the entrance of the estuary to more than 70 m further from the estuary. The isobaths are approximately northeast-southwest, parallel to the coastline, with a strong cross-shelf topographic gradient. The overall oceanic circulation in this estuary-shelf system is highly variable in space and time due to the multiple forcings of wind, river discharge, tide, and land-

* Corresponding author. Department of Ocean Science, The Hong Kong University of Science and Technology & Southern Marine Science and Engineering Guangdong Laboratory, Zhuhai, China.
E-mail address: magan@ust.hk (J. Gan).

https://doi.org/10.1016/j.ecss.2022.108091
Received 14 February 2022; Received in revised form 16 August 2022; Accepted 26 September 2022
Available online 30 September 2022

air-sea interaction (Lai et al., 2021). Seaward gravitational convection characterizes the circulation inside the PRE and competing gravitational convection and intrusive geostrophic currents from the shelf govern the circulation in the lower estuary (Zu et al., 2014). A down-estuary wind enhances the stratification and strengthens the along-estuary exchange circulation via wind straining, and an up-estuary wind increases the vertical mixing and decreases the estuarine circulation (Lai et al., 2018; Pan et al., 2020). Over the entire NSCS, coastal downwelling and upwelling dynamics are strongly controlled by the alongshore wind stress magnitude and wind stress curl (Gan et al., 2015). The southwesterly/northeasterly wind-driven upwelling/downwelling currents spread the freshwater Pearl River plume eastward/westward over the shelf. Accurately representing the wind forcing when modeling this coupled estuary-shelf system is critical to properly simulating the ocean circulation dynamics (Jiang and Xia, 2016).

High-resolution atmospheric forcing is important to accurately

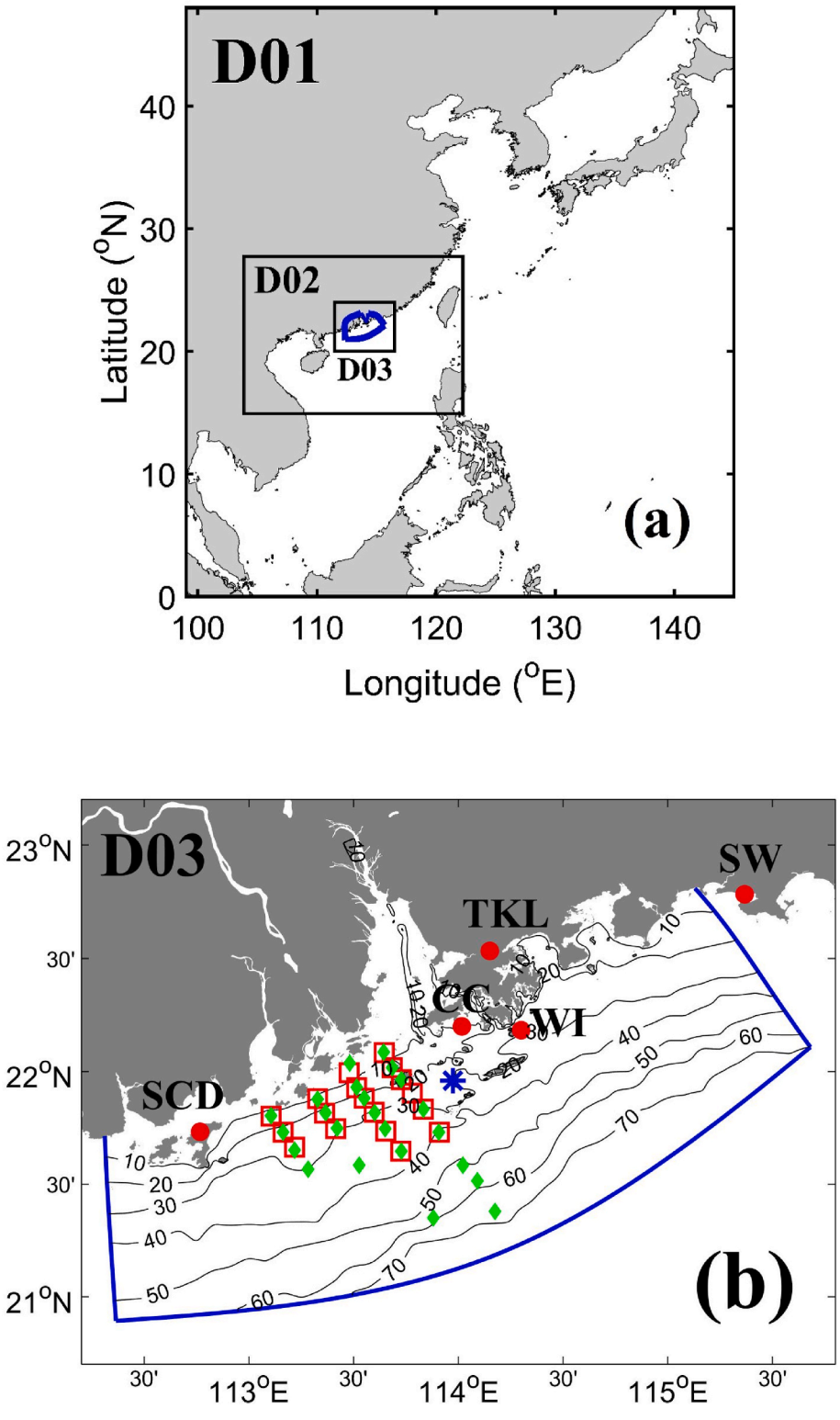

Fig. 1. (a) The model domains of the WRF and PRE ocean models. The area outlined in blue denotes the domain of the PRE ocean model. (b) The inner domain D03 of WRF and the domain of the PRE ocean model with bathymetry (black contour lines). The red dots indicate the atmospheric observation stations at Shan Wei (SW), Shang Chuan Dao (SCD), Cheung Chau (CC), Waglan Island (WI), and Ta Kwu Ling (TKL). The red squares and green diamonds denote the CTD stations. The blue star presents the location of the buoy. (For interpretation of the references to colour in this figure legend, the reader is referred to the Web version of this article.)

simulate ocean circulation (Julie Pullen, 2003; Béranger et al., 2010; Herrmann et al., 2011). Atmospheric forecasting skill improves as the atmospheric model's resolution increases, and more specific topographic features (Cavaleri and Bertotti, 2004; Ágústsson and Ólafsson, 2007; Albert et al., 2010) and mesoscale processes (Béranger et al., 2010) are resolved. High-resolution atmospheric forcings improved the ocean circulation simulations due to better representing the oceanic mixed-layer characteristics and dynamics (Estournel, 2003; Langlais et al., 2009), turbulent heat flux (Akhtar et al., 2017), oceanic response to large wind variability (De Mey et al., 2017), and thermohaline circulation (Castellari et al., 2000; Artale et al., 2016).

The effects of atmosphere-ocean interaction and feedback become more important in an ocean simulation as the grid resolution increases. The local impacts are generated by sub-mesoscale and mesoscale SST variations that alter heat fluxes and winds (Boe et al., 2011), which, in turn, affect the multi-scale circulation in open ocean frontal zones (Chelton et al., 2004; O'Neill et al., 2010) and coastal upwelling regions (Chelton et al., 2007; Desbiolles et al., 2014; Oerder et al., 2016, 2018). Many studies have shown that surface wind and heat fluxes are improved in simulations when air-sea interactions are included in the modeling (Pullen et al., 2006; Seo et al., 2007; Warner et al., 2008; Ricchi et al., 2016; Sun et al., 2020).

How the processes and dynamics of the coastal circulation in the estuary-shelf system of the PRE and NSCS respond to spatiotemporally varying mesoscale and sub-mesoscale wind forcings has not been fully explored by researchers. Furthermore, the effects of land-air-sea interactions on the circulation in the estuary-shelf system have rarely been investigated for the PRE and other similar systems around the world. The main objectives of this paper are: (1) to assess the impact of using high-resolution modeling on coastal meteorology and the response of the coastal ocean to high-resolution wind forcing, and (2) to investigate the impact of the air-sea coupling relative to one-way coupling (forced-mode ocean simulation) and to explore the potential effects of air-sea coupling on coastal circulation dynamics. Investigating how oceanic processes and the underlying dynamics respond to high-resolution atmospheric forcing and atmosphere-ocean coupling would advance physical and numerical understanding of these systems and improve coastal ocean modeling skills.

2. Model configuration and data

2.1. Model configuration and experiments

The Coupled Ocean-Atmosphere-Wave-Sediment Transport (COAWST) modeling system (Warner et al., 2010) was employed to simulate the estuary-shelf hydrodynamic environment of the PRE and NSCS. The ocean model in the COAWST modeling system is the Regional Ocean Modeling System (ROMS), which is a free-surface, hydrostatic, primitive equation model discretized with a vertical coordinate system that follows the terrain (Shchepetkin and McWilliams, 2005).

Our model domain consisted of a horizontally discretized matrix with 400 × 441 points covering the PRE and the shelves off Guangdong in the NSCS (Fig. 1). An orthogonal curvilinear coordinate system followed the coastline. The ultrahigh resolution grid (~0.1 km) resolved the estuary and the inner shelf neighboring Hong Kong. The grid size gradually increased to ~1 km over the shelf at the domain's southern boundary. The topography had been smoothed by using a 2D Shapiro filter. The model had 30 vertical levels and adopted higher resolutions (<0.2 m) in the surface and bottom boundary layers to better resolve the dynamics in these layers. The 2.5-level sub-model for turbulent kinetic energy equations in Mellor and Yamada (1982) was used to parameterize the vertical mixing and diffusion. Horizontal mixing/diffusion was computed using a harmonic scheme with a constant horizontal viscosity/diffusion coefficient (5 m^2 s^{-1}). A third-order upstream bias advection scheme was adapted to solve the horizontal advection in the momentum equations, while the transport of temperature and salinity was solved using the Multidimensional Positive Definite Advection Transport Algorithm by Smolarkiewicz (1984). The dynamical time-step of the ocean model was 30 s. We applied the new tidal and subtidal open boundary condition scheme developed by Liu and Gan (2016, 2020), and we applied tidal forcing to the open boundary using eight major tidal constituents: M2, K1, S2, O1, N2, P1, K2, and Q1. We used the Oregon State University Tidal Inversion Software (Egbert and Erofeeva, 2002) to extract the tidal constituents.

Results from two experiments that differed only by the atmospheric forcing allowed us to assess how our ocean model responded to two different wind forcings with different horizontal resolutions. In the first experiment, referred to as LR-ERAI, we used atmospheric forcing from the Re-Analyses ERA-interim data from the European Centre for Medium-Range Weather Forecasts (ECMWF) which had a spatial resolution of approximately 79 km and 60 vertical levels up to 0.1 hPa. In the second experiment, referred to as HR-WRF, we used higher resolution wind forcing from the regional atmospheric Weather Research and Forecasting (WRF) model (Michalakes et al., 1998). WRF adopts a fully compressible non-hydrostatic model with an Arakawa-C grid in the horizontal direction and terrain-following quality coordinates in the vertical direction. A dynamical downscaling technique was employed in the WRF model to obtain a higher-resolution output (Caldwell et al., 2009), which can reflect the impacts of complex fine topography and land-sea-air interactions. A three-domain-nested configuration was adopted in this study (Fig. 1a). The outer domain of the atmospheric model, D01, covered the western Pacific Ocean, the entire China Sea, and the Japanese Sea, with a horizontal resolution of 9 km. The middle domain, D02, covered the NSCS with a horizontal resolution of 3 km. And the inner domain, D03, covered the Guangdong-Hong Kong-Macao Greater Bay Area and the PRE with a horizontal resolution of 1 km. D03 covered the domain of our coastal ocean model. The U.S. Geological Survey provided the static fields, such as land use and topographic data, with a horizontal grid spacing of 30 arc seconds (approximately 0.9 km). All three domains had 33 layers in the vertical, and the maximum top pressure reached 50 hPa. The initial conditions and lateral boundary conditions for the outer domain were from ERA-interim data provided by the ECMWF. The physics options of WRF included the WSM6 microphysics scheme (Hong et al., 2006a), RRTM longwave radiation scheme (Mlawer et al., 1997), Dudhia shortwave scheme (Dudhia, 1989), YSU boundary layer scheme (Hong et al., 2006b), and the Kain-Fritsch cumulus scheme (Kain, 2004). We performed this experiment offline or in a one-way mode for which the atmospheric model ran first and then used the high-resolution near-surface wind to drive the ocean model. The variables describing the surface heat budget were consistent with the LR-ERAI experiment from the ECMWF and drove the ocean model as a surface boundary condition using the "flux formulation" method (Oerder et al., 2016). The SST from the ERA-interim data was used to act as the boundary forcing for the atmosphere model. We interpolated the results from D03 onto the grid of the PRE ocean model.

We conducted a third experiment as an air-sea two-way fully coupled experiment using the WRF and ROMS models in the COAWST. We called this third experiment CPL-AO. The coupler is the Modelling Coupling Toolkit (MCT; Larson et al., 2005), which is an open-source software library for constructing parallel coupled models from individual parallel models. Each separate model ran on its own set of processors. MCT provides the protocols for inter-model data coupling, allowing efficient data transfer between the different models, and provides interpolation algorithms for the data fields that are transferred. In the WRF-ROMS coupled model, the surface wind stress component, atmospheric pressure, relative humidity, air temperature, cloud fraction, precipitation, and the net shortwave and longwave fluxes from the D03 domain of the atmospheric model were passed to the PRE ocean model. The ocean model passed the simulated SST to the atmospheric model. The momentum and heat fluxes at the ocean-atmosphere interface were computed by WRF, ensuring that both models used the same fluxes. The models exchanged data every 10 min. The solo configurations for the

atmospheric and oceanic models were consistent with the settings of the HR-WRF experiment. We spun up the ocean model with temperature and salinity from May 1, 2015 obtained from a well-validated larger-scale model over the entire northern South China Sea shelf (Gan et al., 2015). Atmospheric forcing from 10 to July 28, 2015 was applied to the ocean model simulation, covering variable upwelling- and downwelling-favorable winds during the field survey period.

2.2. Observations for validation

We obtained hourly surface wind vector and temperature data for the weather stations (Fig. 1b) around PRE from the Hong Kong Observatory (HKO) and the Integrated Surface Database (ISD; Smith et al., 2011; https://www.ncdc.noaa.gov/isd), from the National Centers for Environmental Information (NCEI), National Oceanic and Atmospheric Administration (NOAA). We used this hourly data to validate the atmospheric forcing.

To validate the ocean model, we used conductivity-temperature-depth (CTD) data collected during a survey from 18 to July 22, 2015. A Sea-Bird SBE25 CTD profiling system measured the in-situ salinity and temperature. The CTD stations were along transects in the PRE and over the adjacent shelf as shown in Fig. 1b. We extracted temperature and salinity profiles from the model results at the same locations as the CTD stations to validate our ocean model. At the same time, we conducted a time-series measurement of current using a buoy mooring located in the south of the PRE mouth (Fig. 1b). Additionally, we obtained the Operational SST and Sea Ice Analysis (OSTIA) SST data (http://ghrsst-pp.metoffice.gov.uk/ostia-website/index.html) from the National Centre for Ocean Forecasting of the Met Office (United Kingdom) (Donlon et al., 2012) to validate the SST of the ocean simulation. The OSTIA SST data are from a global daily analysis with a 0.05° × 0.05° horizontal resolution.

3. Model validation

3.1. Atmospheric validation

We compared the observations from HKO and ISD to the atmospheric models' wind fields and air temperatures. Fig. 2 shows the alongshore and cross-shore winds and air temperatures at the Waglan Island (WI) and Ta Kwu Ling (TKL) stations from the observations, the ERA-interim data (ERAI), uncoupled WRF model, and the air-sea coupled model. The alongshore and cross-shore components are the wind vectors rotated by an angle of 23° and are approximately parallel and perpendicular to the coastline, respectively. The positive/negative values of the alongshore wind indicate the upwelling/downwelling-favorable winds.

At the WI station, the relatively weak upwelling-favorable wind prevailed from July 13 to 17 (Fig. 2a), and the wind reversed to blow southwestward (downwelling-favorable) from July 18 to 19 and then rapidly reverted to northeastward (upwelling-favorable) after July 20. The alongshore and cross-shore winds from the low-resolution model (ERA-interim data) underestimated the downwelling-favorable wind on July 19 (Fig. 2a and c). In comparison, the alongshore winds from both the uncoupled and coupled WRF models were all stronger and more consistent with the observations in magnitude on July 19 (Fig. 2a). In the cross-shore direction, the air-sea coupled model agreed best with the observations at the WI station (Fig. 2c). For the TKL station located north of Hong Kong, the intensities of the alongshore and cross-shore winds

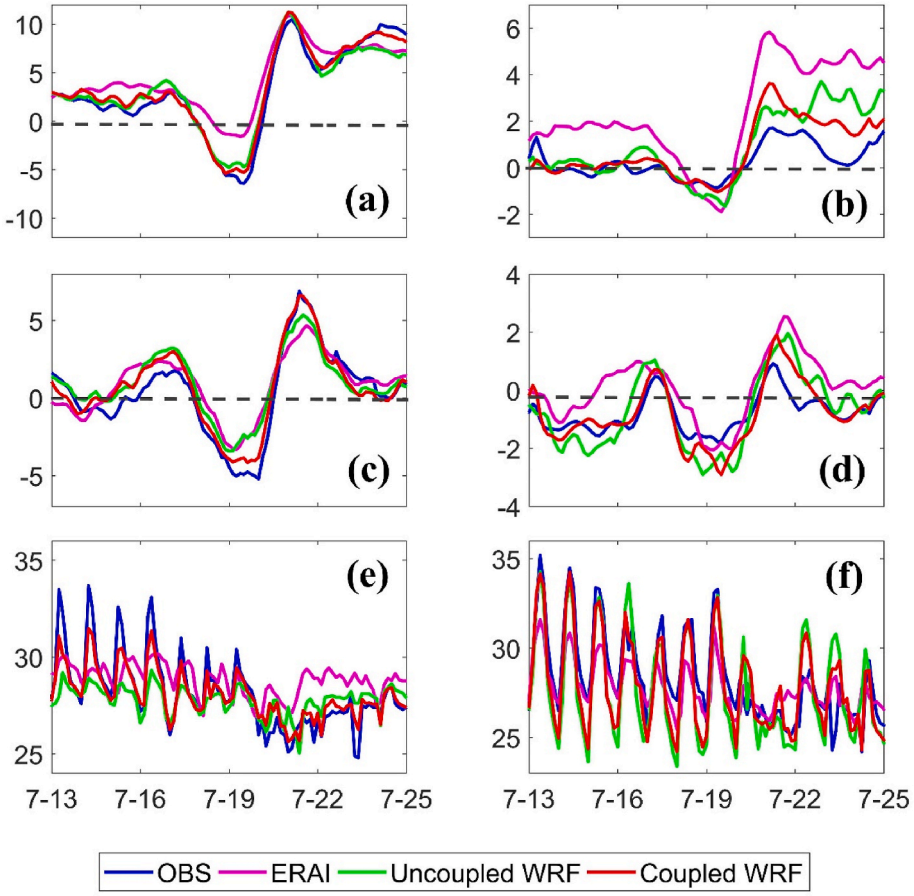

Fig. 2. Comparisons of the (a, b) alongshore and (c, d) cross-shore winds (ms^{-1}) and (e, f) air temperature (°C) of the observations, ERA-Interim data, uncoupled WRF, and coupled WRF models at Waglan Island (a,c,e) and Ta Kwu Ling (b,d,f) stations. The negative value of the alongshore wind in Fig. 2a indicates a downwelling-favorable wind, and the positive value indicates an upwelling-favorable wind.

from the low-resolution ERA-interim data were much stronger than the intensities of the winds from the high-resolution models (Fig. 2b and d) due to the models' underestimating the effects of topography. The station-averaged, including Waglan Island, Ta Kwu Ling, Shan Wei, Shang Chuan Dao, and Cheung Chau stations, root-mean-square errors (RMSE) of the alongshore and cross-shore winds from the air-sea coupled model were 1.78 m/s and 1.46 m/s, respectively, which were smaller than the RMSEs from the ERA-interim data and the uncoupled WRF model (Table 1). In addition, the station-averaged correlation coefficients of the alongshore and cross-shore winds for the air-sea coupled model were the largest (Table 1).

Due to different land uses at the WI and TKL stations, the performances of simulated air temperature are different because they represent processes of the ocean-air and land-air interaction, respectively. The simulated maximum temperatures at the WI station were generally lower than the observations for different wind forcings before July 19 (Fig. 2e), while the simulation of air temperature in the coupled model was improved by considering air-sea interaction with a better SST feedback. After July 19, the uncoupled WRF and air-sea coupled models successfully reproduced the synoptic reduction of temperature, but the low-resolution ERA-Interim data overestimated the air temperature. At the TKL station, the diurnal variation of the air temperature was more consistent with the observation in the air-sea coupled model (Fig. 2f) with a correlation coefficient of 0.86 and an RMSE of 1.43 °C. The station-averaged RMSEs of the air temperature were 1.60, 1.53, and 1.23 °C in the low-resolution model, high-resolution uncoupled model, and air-sea coupled model (Table 1), respectively. The station-averaged correlation coefficient between the modeled and observed air temperature increased from 0.63 in the low-resolution model to 0.83 in the air-sea coupled model (Table 1). Overall, the results from the air-sea coupled model agreed the best with the observations.

Table 1
The RMSE and correlation coefficient of alongshore and cross-shore winds and air temperature from the ERA-Interim data, uncoupled WRF, and coupled WRF models at the Waglan Island and Ta Kwu Ling observation stations, and all stations average.

	Variable	Forcing	Waglan Island	Ta Kwu Ling	All Stations Average
RMSE	Along-Shore Wind (ms^{-1})	ERA-interim	3.27	3.08	2.77
		Uncoupled WRF	2.56	1.68	2.05
		Coupled WRF	2.07	1.62	1.78
	Cross-Shore Wind (ms^{-1})	ERA-interim	2.79	1.61	2.23
		Uncoupled WRF	2.16	1.46	1.74
		Coupled WRF	1.84	1.11	1.49
	Temperature (°C)	ERA-interim	1.78	1.66	1.60
		Uncoupled WRF	1.36	1.83	1.53
		Coupled WRF	1.05	1.43	1.23
Correlation Coefficient	Along-Shore Wind	ERA-interim	0.87	0.49	0.75
		Uncoupled WRF	0.89	0.62	0.80
		Coupled WRF	0.93	0.67	0.84
	Cross- Shore Wind	ERA-interim	0.70	0.52	0.62
		Uncoupled WRF	0.84	0.74	0.78
		Coupled WRF	0.88	0.76	0.82
	Temperature	ERA-interim	0.48	0.82	0.63
		Uncoupled WRF	0.74	0.78	0.73
		Coupled WRF	0.89	0.86	0.83

3.2. Ocean model validation

We used T-S diagrams of sea surface temperature and salinity from the CTD observations (Fig. 1b) and the numerical simulations in the LR-ERAI, HR-WRF, and CPL-AO experiments to assess the performance of the ocean model under different atmospheric forcings (Fig. 3). The ocean model driven by the ERA-interim data (LR-ERAI experiment) overestimated the SST at most stations (Fig. 3a) with an RMSE of 1.48 °C (Table 2). When the ocean model was driven by the high-resolution wind forcing (HR-WRF experiment), the near-surface water was colder (Fig. 3b), and the SST was even further reduced in the air-sea coupled model (CPL-AO experiment in Fig. 3c). The RMSEs of SST in the HR-WRF and CPL-AO experiments were 1.29 and 1.11 °C, respectively, and decreased by 12.8% and 25.0% compared to the LR-ERAI experiment. Meanwhile, the ocean model underestimated the sea surface salinity in the LR-ERAI experiment, especially in the coastal regions where the differences between modeled and observed salinity reached 10 psu (Fig. 3a). The sea surface salinity in the HR-WRF and CPL-AO experiments agreed with the observations better (Fig. 3b and c). The RMSEs of the sea surface salinity in the HR-WRF and CPL-AO experiments, relative to the LR-ERAI experiment, decreased by 23.7% and 28.3% (Table 2), respectively.

Fig. 4 shows the time-averaged SST obtained from the OSTIA remote

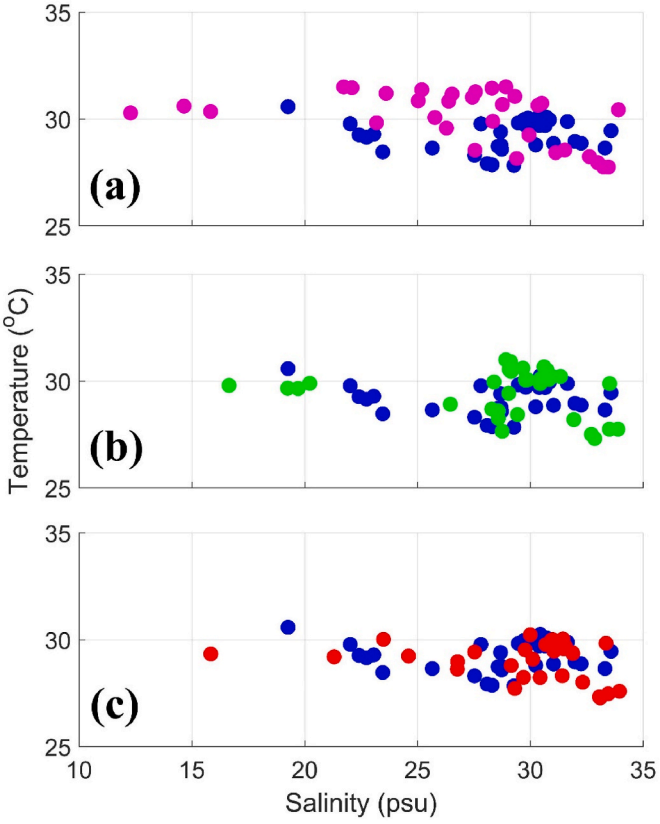

Fig. 3. T-S diagrams of the sea surface temperature and salinity at all the CTD station locations mapped from the LR-ERAI (a), HR-WRF (b), and CPL-AO (c) experiments. The blue dots represent the observed data. (For interpretation of the references to colour in this figure legend, the reader is referred to the Web version of this article.)

Table 2
RMSE of sea surface temperature and salinity in the CTD observations from the LR-ERAI, HR-WRF, and CPL-AO experiments.

Variable	Experiment	LR-ERAI	HR-WRF	CPL-AO
Sea Surface Temperature	RMSE (°C)	1.48	1.29	1.11
	Improvement	/	12.8%	25%
Sea Surface Salinity	RMSE (psu)	1.73	1.32	1.24
	Improvement	/	23.7%	28.3%

sensing observations and the model results from the LR-ERAI, HR-WRF, and CPL-AO experiments from 13 to July 18, 2015. The belt of cold water on the eastern side of the observed SST distribution was evidence of upwelling circulation (Fig. 4a). A warm bias relative to the OSTIA SST was on the western side and was near the coastal regions in the LR-ERAI experiment (Fig. 4b). The simulated SST cooled over the shelf when we applied the high-resolution wind forcing in the HR-WRF experiment (Fig. 4c) due to the increased vertical mixing induced by the strengthened wind stress (Figure not shown). However, due to the weaker wind stress near Hong Kong Island, the SST over the eastern cold-water belt in the HR-WRF experiment was slightly warmer than that in the LR-ERAI experiment. The SST bias decreased further when we coupled the regional ocean and atmospheric models in the CPL-AO experiment (Fig. 4d). In general, the SST from the CPL-AO experiment agreed the best with the observed SST from OSTIA.

The time series of depth-averaged zonal and meridional velocities from both the buoy observation (Fig. 1b) and the LR-ERAI, HR-WRF, and CPL-AO experiments are shown in Fig. 5. The depth-averaged zonal and meridional velocities exhibited an extensive fluctuation during the extensive upwelling-favorable wind. The biases of zonal velocities were larger in the LR-ERAI and HR-WRF experiments from July 23 to 25. In the coupled model, the biases of zonal velocity decreased. The meridional velocities were similar among these three experiments. The observation-model correlation of zonal velocity was improved from 0.72 in the LR-ERAI to 0.81 in the CPL-AO experiment (Table 3). Meanwhile, the RMSEs of zonal velocity reduced from 0.087 ms^{-1} to 0.053 m/s. For the meridional velocity, the correlation was the highest and the RMSE was the lowest in the CPL-AO experiment.

In short, the high-resolution air-sea coupled model resolved the local dynamic effects induced by the topography and small-scale physical processes better. In addition, with the consideration of air-sea interaction, the air-sea coupled model also had a better representation of the wind forcing, which significantly improved the accuracy of the simulated coastal currents, surface water temperature, and salinity.

4. Results

At the beginning of the field cruise in the PRE region, there was a relatively weak upwelling-favorable wind. Then, around July 19, there was extensive short-term downwelling-favorable wind followed by strong upwelling-favorable wind after July 20 (Fig. 2a). We mainly focused on the response of the coastal ocean circulation to the upwelling-favorable wind from July 20 to 28 in these three experiments.

4.1. Surface circulation

Coastal upwelling dynamics are strongly controlled by alongshore wind stress and wind stress curl. The time-averaged wind stress and wind stress curl from the ERA-interim reanalysis data (used in the LR-ERAI experiment), the high-resolution uncoupled WRF model (used in the HR-WRF experiment), and the air-sea coupled model (used in the CPL-AO experiment) are shown in Fig. 6 when the upwelling-favorable wind occurred from 20 to 28 July. The intensity of the wind stress from the ERA-interim reanalysis data was relatively weak (Fig. 6a), but it strengthened in the simulation from the high-resolution uncoupled WRF model (Fig. 6c), especially over the shelf region. The wind stress curl in the ERA-interim data was generally positive and spatially uniform over the shelf due to the lower resolution of the data (Fig. 6b). The pattern of the wind stress curl was more complex in the high-resolution model than that in the low-resolution model. The wind stress curl intensified near the coast in the high-resolution WRF model, which resolved the spatial variability of the wind stress better. In the high-resolution WRF results, the distinct negative wind stress curl outside the estuary and positive around the whole domain were obvious in Fig. 6d. In the air-sea coupled model's results, the patterns of wind stress and wind stress curl were like the patterns seen in the uncoupled WRF model results but were slightly

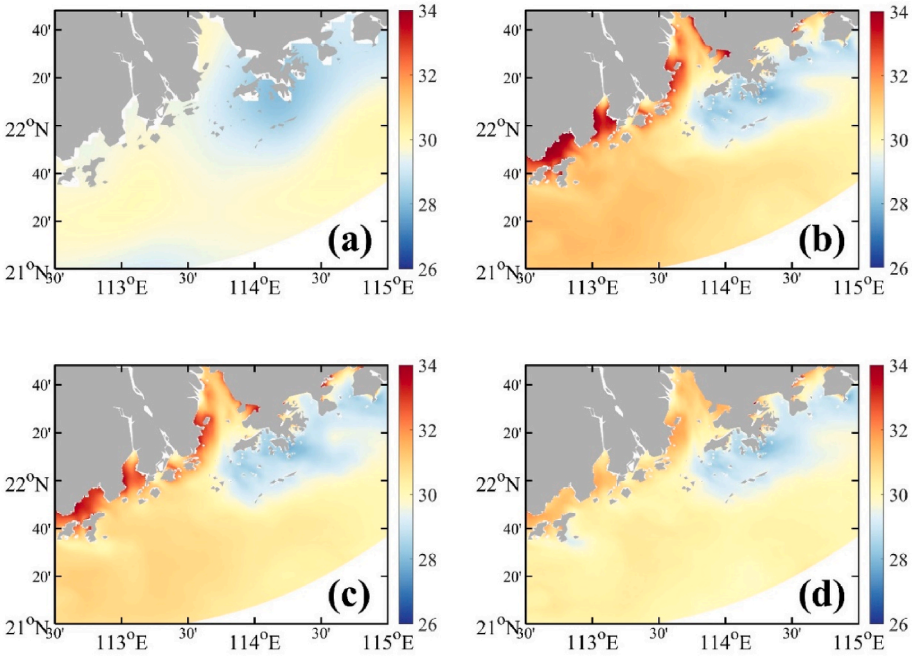

Fig. 4. The time-averaged of the SST (°C) from the (a) OSTIA remote sensing observation and the (b) LR-ERAI, (c) HR-WRF, and (d) CPL-AO experiments from July 13 to 18.

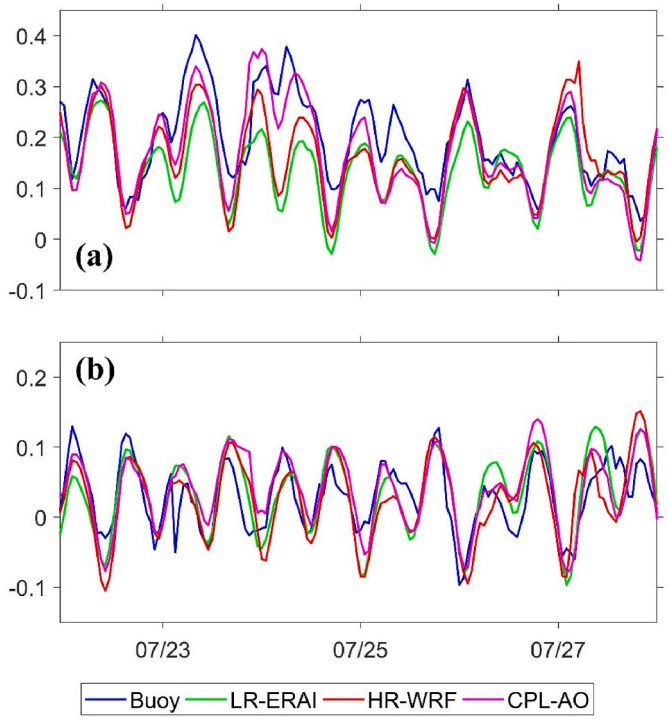

Fig. 5. Time series of depth-averaged (a) zonal and (b) meridional velocities from the buoy observation, the LR-ERAI, HR-WRF, and CPL-AO experiments.

Table 3
RMSE and correlation coefficient (CC) of depth-averaged zonal and meridional velocities between the buoy observation and the LR-ERAI, HR-WRF, and CPL-AO experiments.

Variable	Experiment	LR-ERAI	HR-WRF	CPL-AO
zonal velocity	RMSE	0.087	0.071	0.053
	CC	0.72	0.75	0.87
meridional velocity	RMSE	0.044	0.042	0.036
	CC	0.67	0.67	0.74

weaker and homogeneous (Fig. 6e and f).

With the upwelling-favorable wind, a northeastward upwelling jet over the shelf appeared in the surface currents near the PRE (Fig. 7a). Compared to the LR-ERAI experiment, the surface eastward currents intensified over the inner shelf in the HR-WRF experiment due to the strengthened nearshore wind stress (Fig. 7b). Due to the weaker wind stress in the CPL-AO experiment, the surface eastward currents were slightly weaker near the western shore and over the eastern shelf, compared to the HR-WRF experiment (Fig. 7c).

The surface salinity in the region is characterized by the offshore movement of the Pearl River plume. In the LR-ERAI experiment, when the extensive southwesterly winds prevailed, the freshwater from the estuary advected eastward and offshore (Fig. 7d). The 32 psu surface salinity contours suggest more freshwater was constrained on the west side of the PRE due to the strengthened eastward alongshore jet in the HR-WRF and CPL-AO experiments (Fig. 7d). The surface salinity patterns in the results from the HR-WRF and CPL-AO experiments were similar, but in the HR-WRF experiment, more freshwater was constrained inside the PRE, indicating the presence of a strengthened upwelling jet.

4.2. Cross-isobath transport

To illustrate the response of the cross-shelf exchanges to the different atmospheric forcings, we examined the cross-isobath components of the depth-averaged and bottom velocities over the 10m–50m isobaths by projecting the simulated velocities onto the cross-isobath direction (Fig. 8). We defined the orientation of the isobath in the computational domain as the inverse tangent of the northward and eastward gradients of the topography. A positive (negative) value represented an onshore (offshore) transport of the shelf water normal to the isobath. Based on the strength of the transport in different regions of our model domain, we divided the domain around the PRE into three regions (Fig. 8a). In the west, we defined Region C1 to be near the coast from the 10m–30m isobaths. Region C2 was on the shelf from the 30m–50m isobaths. Region E was in the east from the 20m–50m isobaths. The final region was in the center, but due to the influence of the complex topography and islands, we excluded the discussion of cross-isobath transport in the center region from this study.

During the upwelling-favorable wind, the depth-averaged cross-isobath transports clearly showed a net offshore transport for Region C1 and Region C2, and there was an onshore invasion on the eastern side for Region E in the three experiments. At the same time, predominant onshore transports occurred over the bottom layer due to the upwelling-favorable wind (Fig. 8d and e). In the LR-ERAI experiment, the depth-averaged cross-isobath transports, including onshore transport in Region E and offshore transports in Region C1 and C2, were weaker than the depth-averaged transports in the HR-WRF experiment (Fig. 8b). The bottom onshore transport was strengthened in the HR-WRF experiment (Fig. 8e). The differences between the depth-averaged cross-isobath velocities from the HR-WRF and CPL-AO experiments showed that the cross-isobath transports in the CPL-AO experiment were stronger in Region C2 and Region E but were weaker in Region C1 (Fig. 8c). For the bottom layer, the onshore transport intensified in the HR-WRF experiment when we applied the high-resolution wind forcing (Fig. 8e), but in the CPL-AO experiment, the bottom onshore transport weakened in Region C2 and Region E (Fig. 8f). Adjusting the wind stress in the air-sea coupled model resulted in a moderate bottom onshore transport and depth-averaged cross-isobath transport over the shelf.

Overall, the cross-isobath transport in the HR-WRF experiment was strongest in Region C1, but in Region C2 and Region E, the cross-isobath transports were strongest in the CPL-AO experiment (Fig. 9). However, the cross-isobath transports were weakest for all three regions in the LR-ERAI experiment. We discuss the underlying dynamics of the changing transports in the different experiments in the next section.

5. Analyses and discussion

To better understand the impacts of high-resolution wind forcing and air-sea coupling on the dynamic processes of the cross-isobath transport around the PRE, we used the term balances in the depth-averaged momentum and vorticity equations. With these equations, we examined the dynamic characteristics controlling the processes of the cross-isobath transport.

5.1. Dynamics of cross-isobath transport

We analyzed the forcing mechanisms involved in the cross-isobath transport with the corresponding along-isobath momentum balances. The depth-averaged along-isobath momentum equation is expressed as

$$\overbrace{\frac{\partial \overline{u}}{\partial t}}^{ACCEL} = \overbrace{f\overline{v}}^{COR} \overbrace{-[(\overline{u},\overline{v})\bullet\nabla]\overline{u}}^{HADV} \overbrace{-g\eta^{x}}^{PGF} + \overbrace{\frac{\tau^{sx}}{\rho_0 D}}^{SSTR} \overbrace{-\frac{\tau^{bx}}{\rho_0 D}}^{BSTR} + \overbrace{K_h\nabla^2\overline{u}}^{HVISC} \quad (1)$$

where the superscript, x, denotes the momentum in the along-isobath direction. The variables τ_s and τ_b are the surface and bottom stresses, respectively. The reference density and coefficient of horizontal viscosity are represented by ρ_0 and K_h, respectively. The terms in Equation (1) are acceleration (ACCEL), Coriolis force (COR), horizontal nonlinear

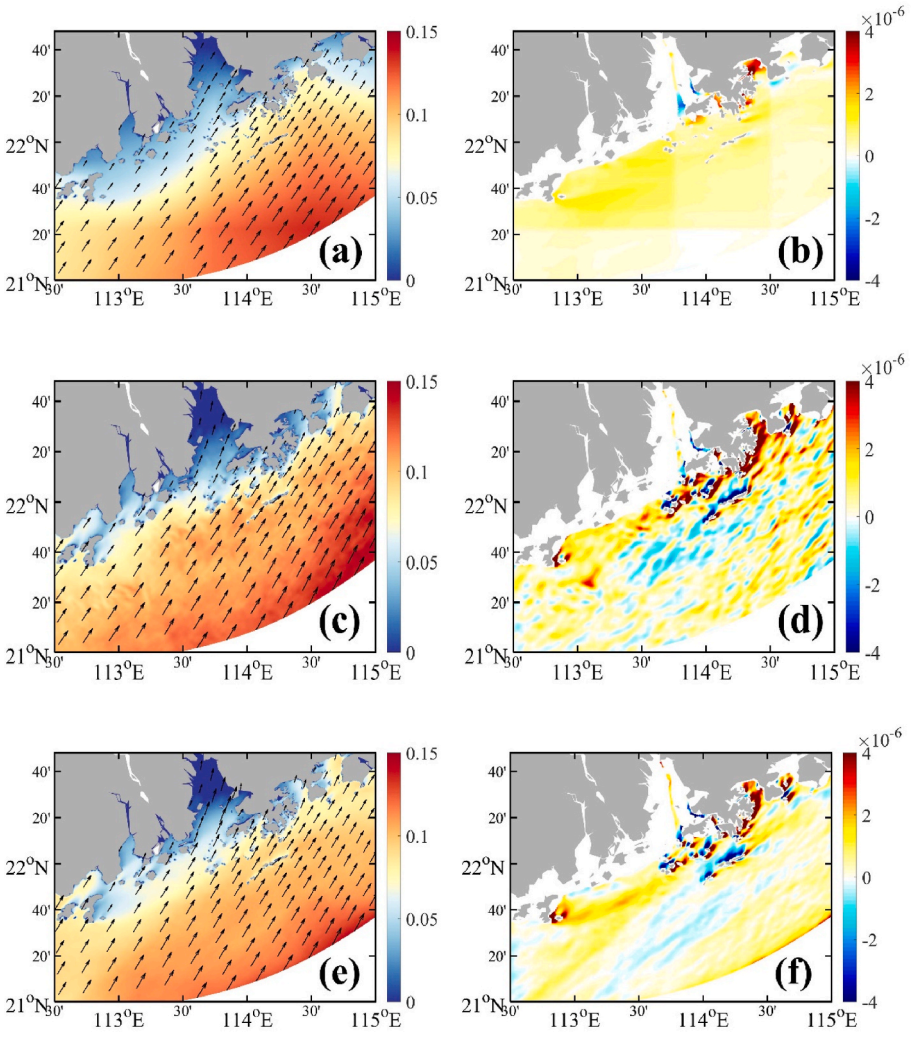

Fig. 6. The time-averaged (a, c, e) wind stress (Pa) and (b, d, f) wind stress curl (Nm^{-3}) from the (a, b) ERA-interim reanalysis data, (c, d) high-resolution uncoupled WRF model, and (e, f) air-sea coupled model during the upwelling-favorable wind.

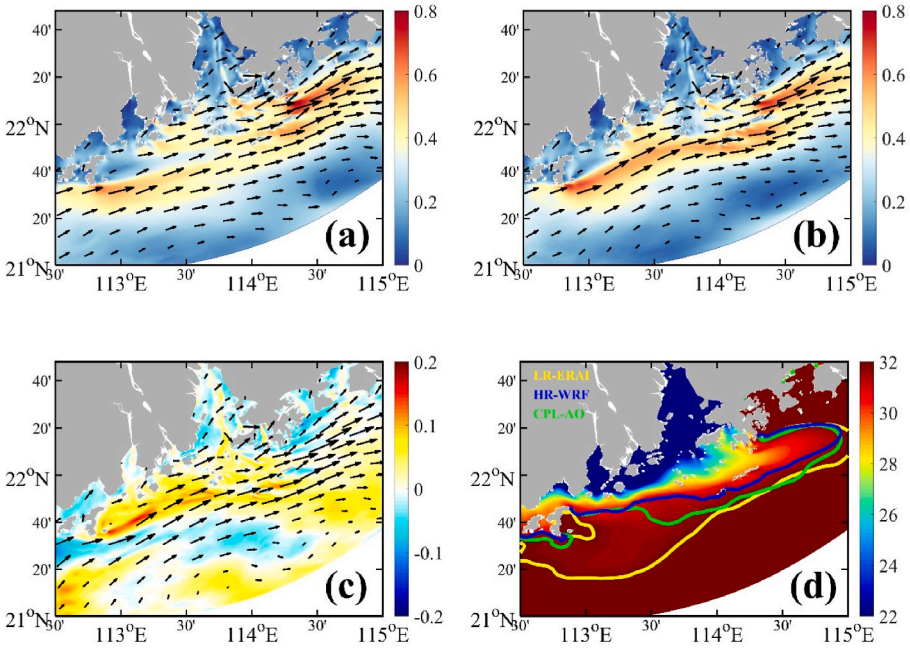

Fig. 7. The time-averaged surface currents (ms^{-1}) in the (a) LR-ERAI and (b) HR-WRF experiments during the upwelling-favorable wind. (c) The difference in the surface currents (ms^{-1}) between the HR-WRF and CPL-AO experiments. (d) The sea surface salinity (psu) in the LR-ERAI experiment. The contour lines of the 32 psμ surface salinity in the LR-ERAI, HR-WRF, and CPL-AO experiments are yellow, blue, and green in Fig. 7d, respectively. (For interpretation of the references to colour in this figure legend, the reader is referred to the Web version of this article.)

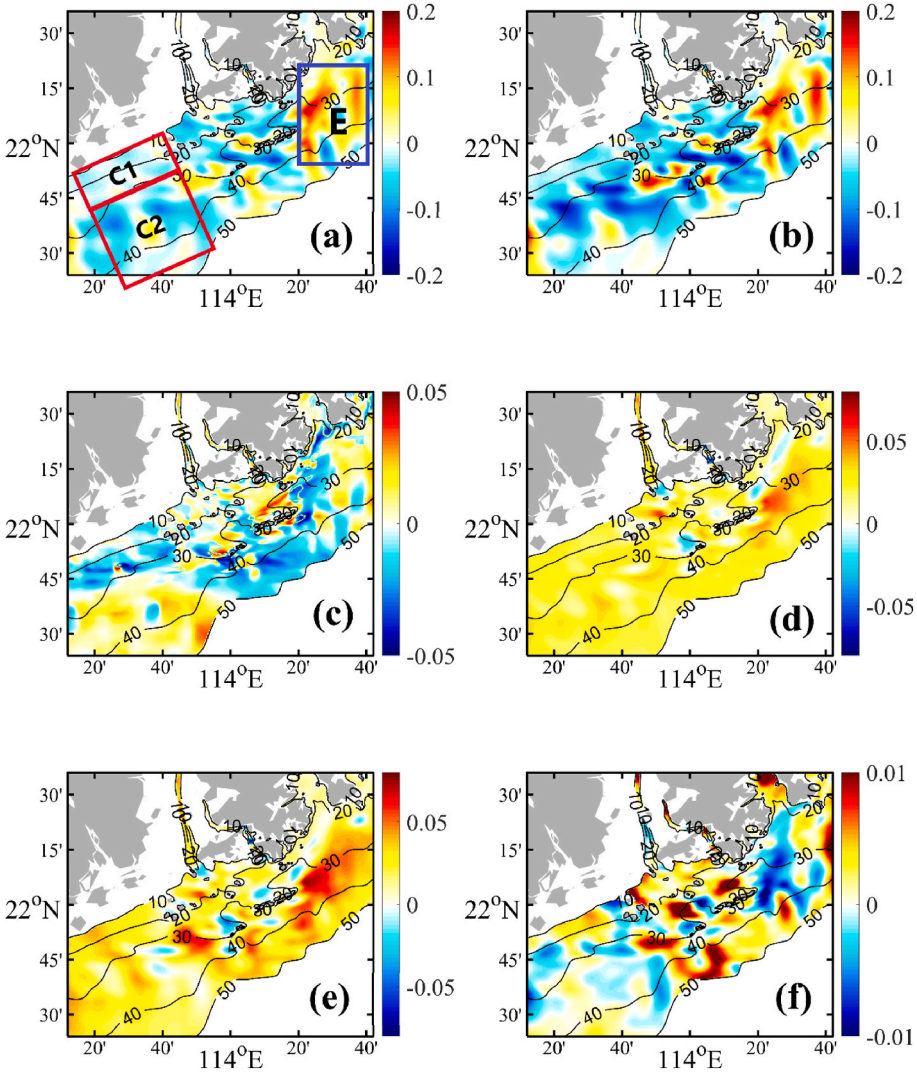

Fig. 8. (a, b) The depth-averaged and (d, e) bottom cross-isobath velocities (ms^{-1}) from the LR-ERAI and HR-WRF experiments during the upwelling-favorable wind. The differences of the (c) depth-averaged and (f) bottom cross isobath velocities (ms^{-1}) between the HR-WRF and CPL-AO experiments during the upwelling-favorable wind. The rectangles in Fig. 8a depict regions C1, C2, and E. A positive (negative) value indicates an onshore (offshore) transport of the shelf water normal to the isobath.

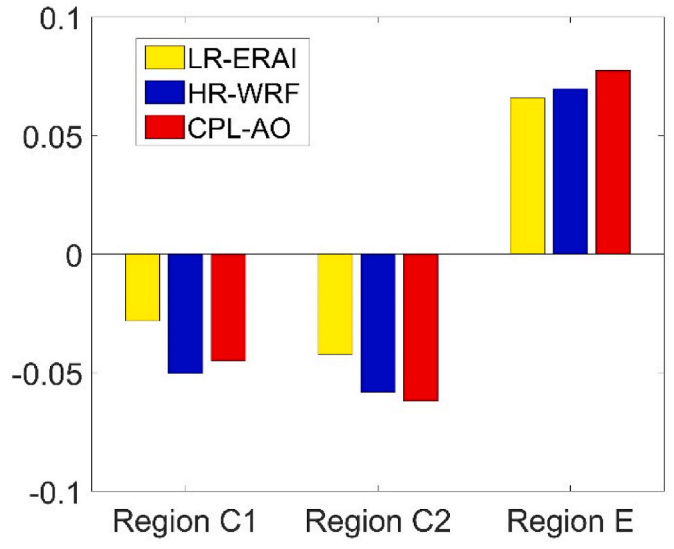

Fig. 9. Domain average of the depth-averaged cross-isobath velocities (ms^{-1}) for regions C1, C2, and E from the LR-ERAI, HR-WRF, and CPL-AO experiments.

advection (HADV), pressure gradient force (PGF), surface wind stress (SSTR), frictional bottom stress (BSTR), and horizontal viscosity (HVISC). We also considered the behavior of the sum of COR and PGF, referred to as the ageostrophic pressure gradient (AGE).

Fig. 10 shows the domain average of the depth-averaged along-isobath momentum terms during upwelling-favorable wind in the regions C1, C2, and E for the LR-ERAI, HR-WRF, and CPL-AO experiments. We neglected the acceleration, HVISC, and HADV terms because they were at least one order of magnitude smaller than the other terms in Equation (1). The main balance along the isobaths in all regions was among the COR, PGF, and SSTR (Fig. 10), in which the BSTR was much smaller, suggesting AGE was primarily balanced by the SSTR to form an Ekman velocity. The intensity of the wind stress mainly determined the offshore transports (COR<0) in regions C1 and C2 (Fig. 10a and b). Compared with the LR-ERAI experiment, the offshore transports were stronger in regions C1 and C2 in the HR-WRF experiment due to the intensified wind stress. Although the SSTR was larger in the HR-WRF in Region C2, the offshore transport was weaker than that in the CPL-AO experiment (Fig. 10b), in which an intensified along-isobath PGF enhanced the offshore transport. In Region E, the intensity of the negative along-isobath PGF mainly determined the onshore transport (COR>0), and the SSTR was the second largest contributor (Fig. 10c), suggesting a geographic current. Although the SSTR was weaker in the CPL-AO experiment, the intensified westward along-isobath PGF resulted in a stronger onshore transport.

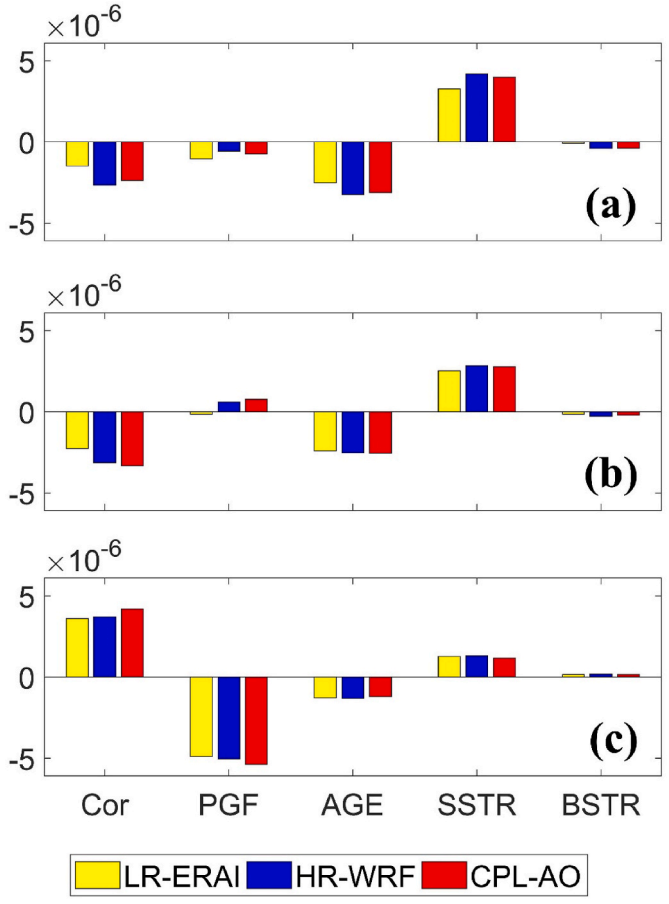

Fig. 10. Domain average of the depth-averaged along-isobath COR, PGF, AGE, SSTR, and BSTR (ms^{-2}) from the LR-ERAI, HR-WRF, and CPL-AO experiments for regions (a) C1, (b) C2, and (c) E during the upwelling-favorable wind.

5.2. Dynamics of along-isobath PGF

We identified that wind stress and along-isobath PGF mainly determined how intensely the different forcings influenced the cross-isobath transports. As we mentioned before, the along-isobath PGF intensified under the impact of the air-sea interaction in the CPL-AO experiment. Studies by Chelton et al. (2004), and O'Neill et al. (2005) suggested that the atmospheric response to the fine structure in the SST field might be important to the feedback onto the ocean, particularly through changes in the wind stress curl. Gan et al. (2013) proposed that intensified offshore transport was formed by a strengthened geostrophic transport due to a positive along-isobath PGF, which was generated by the net frictional stress curl in the water column. Based on the linear depth-integrated vorticity equation, Gan et al. (2013) and Liu and Gan (2014) proposed the depth-averaged along-isobath PGF could be decomposed as:

$$\overbrace{\frac{-1}{\rho_0}P_{x*}}^{PGF_{x*}} = \overbrace{\frac{1}{D_{y*}}\nabla\times\left(-\frac{\frac{g}{\rho_0}\int_{-H}^{0} z\rho dz\nabla H}{H}\right)}^{JEBAR} + \overbrace{\frac{1}{D_{y*}}\overline{\nabla}\times\left(\frac{\tau_b}{\rho_0}\right)}^{BSC} + \overbrace{\frac{1}{D_{y*}}\overline{\nabla}\times\left(-\frac{\tau_s}{\rho_0}\right)}^{SSC} + \overbrace{\frac{1}{D_{y*}}J(\psi,\nabla\times\overrightarrow{v})}^{RVA} + \overbrace{\left(\frac{\|\overrightarrow{v}\|^2}{2}\right)_{x*}}^{GMF} \quad (2)$$

where subscripts, x* and y*, denote partial differentiation in the directions along and normal to the isobaths, respectively. The PGF_{x*} represents the along-isobath PGF, which is governed by the joint effect of baroclinic and relief (JEBAR) due to the topography and baroclinicity of waters, and the net stress curl jointly governed by the curl of bottom stress (BSC) and the curl of surface stress (SSC) in the water column, and the nonlinear relative vorticity advection (RVA), as well as the gradient of momentum flux (GMF). GMF is very small compared with the other terms and can be neglected.

Fig. 11 shows the domain average of JEBAR, BSC, SSC, RVA, and depth-averaged along-isobath PGF for Region C1, C2 and Region E in the LR-ERAI, HR-WRF and CPL-AO experiments. A positive value denotes onshore transport. The along-isobath PGF tended to enhance the onshore transport (Fig. 11a) in Region C1, where the along-isobath PGF was mainly determined by the SSC. The along-isobath PGF was larger in the LR-ERAI experiment due to a greater SSC. Although the SSC was weaker in the CPL-AO experiment than that in the HR-WRF experiment, the net stress curl was larger, resulting in a stronger along-isobath PGF in the CPL-AO experiment.

For Region C2, the positive SSC played a predominated role in the LR-ERAI experiment and balanced the other terms, resulting in a weakest along-isobath PGF (Fig. 11b). The along-isobath PGF was mainly contributed by the SSC and RVA in the HR-WRF experiment, while the BSC reduced the along-isobath PGF. In the CPL-AO experiment, the larger RVA due to the combined effect of the eastward shelf current and the along-shore variation of the relative vorticity was the major contributor to the along-isobath PGF. The RVA combined with the JEBAR effect enhanced the cross-isobath water exchange and offset the net stress curl (SSC and BSC) in the CPL-AO experiment, indicating an opposite effect of SSC to the HR-WRF experiment (Fig. 11b).

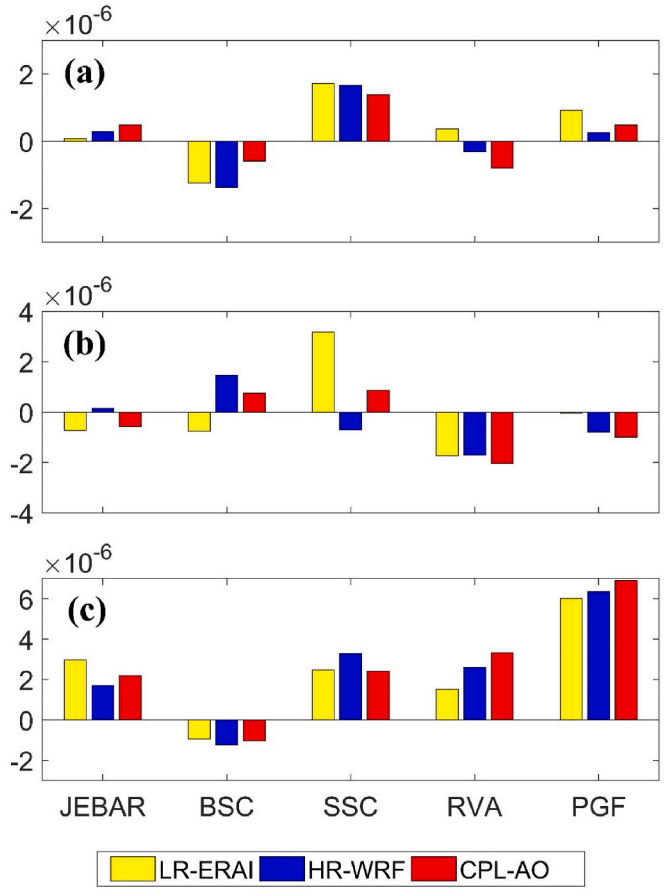

Fig. 11. Domain average of the JEBAR, BSC, SSC, RVA, and depth-averaged along-isobath PGF (ms^{-2}) from the LR-ERAI, HR-WRF and CPL-AO experiments for (a) Region C1, (b) Region C2 and (c) Region E during the upwelling-favorable wind.

In Region E, the positive JEBAR term was the largest due to more eastward expansion of the freshwater in the LR-ERAI experiment, but the SSC and RVA were relatively small, resulting in a weaker along-isobath PGF and onshore transport. The SSC was the largest in the HR-WRF experiment, but the JEBAR and RVA were smaller than those in the CPL-AO experiment, leading to a weaker along-isobath PGF (Fig. 11c). The colder water in the CPL-AO experiment reduced the strength of the surface wind stress curl, but the JEBAR effect and RVA were strengthened. As a result, the along-isobath PGF was strengthened in the air-sea coupled model, resulting in a stronger cross-isobath onshore transport.

Overall, the JEBAR effect was the largest in Region C2 and E due to more offshore expansion of the plume water in the LR-ERAI experiment. Compared with the HR-WRF experiment, the SSC was distinctly influenced by the air-sea coupling and played an important role in determining the along-isobath PGF and cross-isobath transport. The colder near-surface water in CPL-AO tended to reduce the strengths and the variability of surface stress curl for both Region C2 and E when considering air-sea interaction. Furthermore, the enhanced JEBAR effect and RVA in the air-sea coupled model were important to strengthening the cross-isobath transport.

5.3. SST feedback

A key difference in the uncoupled and air-sea coupled models comes from the feedback SST and its impact on wind stress. SST induces the air pressure gradients that affect the atmospheric winds which adjust the ocean via surface wind stress and wind stress curl. Fig. 12 presents the domain average of SST forcing to the atmosphere model, air temperature, and wind stress in the HR-WRF and CPL-AO experiments during the upwelling-favorable wind. In the HR-WRF experiment, the SST forcing from the low-resolution ERA-interim data was greater than in the air-sea coupled model (Fig. 12a), leading to the air temperature in the air-sea coupled model being colder than that in the uncoupled WRF model (Fig. 12b). The surface wind stress was stronger under convectively unstable conditions at high SST when the surface boundary layer in the ocean thickened because of enhanced wind-induced mixing. As a result, the colder water in the air-sea coupled model weakened the surface wind stress, and the uncoupled WRF model generated stronger wind stress (Fig. 12c). Adjusting the SST in the air-sea coupled model, in turn, improved the baroclinicity of the coastal atmosphere and further adjusted the wind stress and cross-shore circulation.

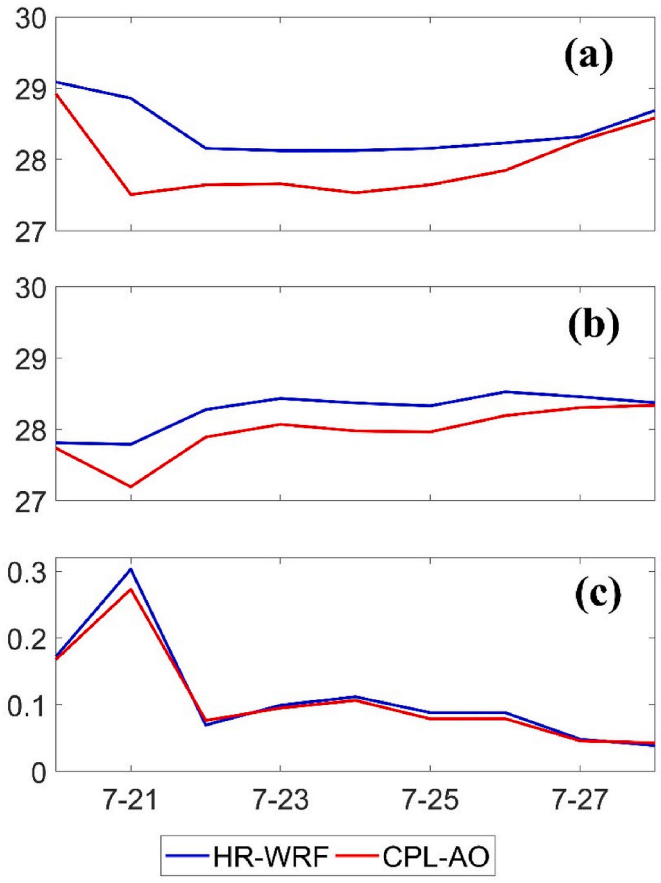

Fig. 12. Time series of the domain-averaged of (a) SST, (b) air temperature (°C), and (c) wind stress (Pa) from the HR-WRF and CPL-AO experiments during the upwelling-favorable wind.

6. Conclusion

Accurately representing the surface heat budget and momentum fluxes is essential to the boundary forcing of an ocean model. Multi-forcings control the coastal ocean where strong land-air-sea interaction poses a great challenge when simulating the atmospheric and ocean, and when the air and sea are coupled in an ocean model. In this study, we investigated the roles of local high-resolution wind forcing in an estuary-shelf ocean simulation and assessed the importance of coastal-scale ocean-atmospheric coupling on the coastal ocean circulation with respect to the coastal circulation's response to an upwelling-favorable wind. In this case, we used the PRE and NSCS as our estuary-shelf system and investigated the ocean response near the PRE. We produced three numerical simulations driven by (1) global reanalysis data from ECMWF, (2) high-resolution wind forcing from an uncoupled regional atmospheric model, and (3) an air-sea coupled model. The three simulations were implemented from 10 to July 28, 2015 covering the same period as an observational cruise. We validated the modeling results using data from weather stations from ISD and in-situ CTD measurements collected during the field cruise in the PRE. Comparing the modeling results with the in-situ observations suggested that the high-resolution atmospheric model significantly improved the simulations of the near-surface wind and air temperature, resulting in improved accuracy of the simulated coastal ocean currents, water temperature, and salinity. The high-resolution air-sea coupled model further improved the atmospheric and oceanic simulations because the air-sea interactions were considered due to the coupling.

In addition, the shelf circulation dynamics were resolved better in the ocean model when driven by high-resolution wind forcing. The high-resolution wind forcing produced strengthened cross-isobath transport due to the enhanced surface wind stress and along-isobath PGF. Compared with the uncoupled model, the depth-averaged cross-isobath transport intensified in the air-sea coupled model due to the enhanced along-isobath PGF. The wind stress curl was distinctly influenced by the air-sea coupling and played an important role in determining the along-isobath PGF and cross-isobath transport. In the air-sea coupled model, the relative vorticity advection strengthened and offset the greater net stress curl for strengthening the along-isobath PGF on the western shelf, and over the eastern shelf, the intensified JEBAR effect and relative vorticity advection in the air-sea coupled model strengthened the along-isobath PGF, resulting in a stronger cross-isobath transport.

The simulated SST was sensitive to the atmospheric forcing and the influence of air-sea coupling in the coastal region. SST was lower when we applied the high-resolution wind forcing rather than the global-scale reanalysis forcing due to the strong vertical mixing induced by the enhanced wind stress from the uncoupled WRF model. The lower SST from the air-sea coupling model fed back to the atmosphere and reduced the air temperature and further adjusted the wind stress and wind stress curl and associated cross-isobath transport. Consequently, the air-sea coupled model represented a major advance in interacting regional atmospheric and oceanic processes to dynamically improve the response of the ocean.

CRediT authorship contribution statement

Wenfeng Lai: Writing – original draft, Validation, Methodology, Investigation, Conceptualization. **Jianping Gan:** Writing – review & editing, Methodology, Conceptualization.

Declaration of competing interest

The authors declare that they have no known competing financial interests or personal relationships that could have appeared to influence the work reported in this paper.

Data availability

Data will be made available on request.

Acknowledgments

This work was supported by Innovation Group Project of Southern Marine Science and Engineering Guangdong Laboratory (Zhuhai) (projects 311020003 and 311021004), the Theme-based Research Scheme (T21-602/16-R, GRF16212720) of the Hong Kong Research Grants Council. We are also grateful for the support of The National Supercomputing Centers of Tianjin and Guangzhou. The data for this study are generated from the publicly distributed Regional Ocean Model System (ROMS, https://www.myroms.org/).

References

Ágústsson, H., Ólafsson, H., 2007. Simulating a severe windstorm in complex terrain. Meteorol. Z. 16 (1), 111–122. https://doi.org/10.1127/0941-2948/2007/0169.

Akhtar, N., Brauch, J., Ahrens, B., 2017. Climate modeling over the Mediterranean Sea: impact of resolution and ocean coupling. Clim. Dynam. 51 (3), 933–948. https://doi.org/10.1007/s00382-017-3570-8.

Albert, A., Echevin, V., Lévy, M., Aumont, O., 2010. Impact of nearshore wind stress curl on coastal circulation and primary productivity in the Peru upwelling system. J. Geophys. Res. 115 (C12) https://doi.org/10.1029/2010jc006569.

Artale, V., Calmanti, S., Sutera, A., 2016. Thermohaline circulation sensitivity to intermediate-level anomalies. Tellus Dyn. Meteorol. Oceanogr. 54 (2), 159–174. https://doi.org/10.3402/tellusa.v54i2.12130.

Béranger, K., Drillet, Y., Houssais, M.-N., Testor, P., Bourdallé-Badie, R., Alhammoud, B., Bozec, A., Mortier, L., Bouruet-Aubertot, P., Crépon, M., 2010. Impact of the spatial distribution of the atmospheric forcing on water mass formation in the Mediterranean Sea. J. Geophys. Res. 115 (C12) https://doi.org/10.1029/2009jc005648.

Boe, J., Hall, A., Colas, F., McWilliams, J.C., Qu, X., Kurian, J., Kapnick, S.B., 2011. What shapes mesoscale wind anomalies in coastal upwelling zones? Clim. Dynam. 36 (11–12), 2037–2049. https://doi.org/10.1007/s00382-011-1058-5.

Caldwell, P., Chin, H.-N.S., Bader, D.C., Bala, G., 2009. Evaluation of a WRF dynamical downscaling simulation over California. Climatic Change 95 (3–4), 499–521. https://doi.org/10.1007/s10584-009-9583-5.

Castellari, S., Pinardi, N., Leaman, K., 2000. Simulation of water mass formation processes in the Mediterranean Sea: influence of the time frequency of the atmospheric forcing. J. Geophys. Res.: Oceans 105 (C10), 24157–24181. https://doi.org/10.1029/2000jc900055.

Cavaleri, L., Bertotti, L., 2004. Accuracy of the modelled wind and wave fields in enclosed seas. Tellus Series a-Dynamic Meteorology and Oceanography 56 (2), 167–175. https://doi.org/10.1111/j.1600-0870.2004.00042.x.

Chelton, D.B., Schlax, M.G., Freilich, M.H., Milliff, R.F., 2004. Satellite measurements reveal persistent small-scale features in ocean winds. Science 303 (5660), 978–983. https://doi.org/10.1126/science.1091901.

Chelton, D.B., Schlax, M.G., Samelson, R.M., 2007. Summertime coupling between sea surface temperature and wind stress in the California current system. J. Phys. Oceanogr. 37 (3), 495–517. https://doi.org/10.1175/jpo3025.1.

De Mey, P., Stanev, E., Kourafalou, V.H., 2017. Science in support of coastal ocean forecasting-part 1. Ocean Dynam. 67 (5), 665–668. https://doi.org/10.1007/s10236-017-1048-1.

Desbiolles, F., Blanke, B., Bentamy, A., 2014. Short-term upwelling events at the western African coast related to synoptic atmospheric structures as derived from satellite observations. J. Geophys. Res.: Oceans 119 (1), 461–483. https://doi.org/10.1002/2013jc009278.

Donlon, C.J., Martin, M., Stark, J., Roberts-Jones, J., Fiedler, E., Wimmer, W., 2012. The operational sea surface temperature and sea Ice analysis (OSTIA) system. Remote Sens. Environ. 116, 140–158. https://doi.org/10.1016/j.rse.2010.10.017.

Dudhia, J., 1989. Numerical study of convection observed during the winter monsoon experiment using a mesoscale two-dimensional model. J. Atmos. Sci. 46, 3077–3107. https://doi.org/10.1175/1520-0469(1989)046<3077:NSOCOD>2.0.CO, 2.

Egbert, G.D., Erofeeva, S.Y., 2002. Efficient inverse modeling of barotropic ocean tides. J. Atmos. Ocean. Technol. 19 (2), 183–204. https://doi.org/10.1175/1520-0426(2002)019<0183:eimobo>2.0.co, 2.

Estournel, C., 2003. Observation and modeling of the winter coastal oceanic circulation in the Gulf of Lion under wind conditions influenced by the continental orography (FETCH experiment). J. Geophys. Res. 108 (C3) https://doi.org/10.1029/2001jc000825.

Gan, J., Wang, J., Liang, L., Li, L., Guo, X., 2015. A modeling study of the formation, maintenance, and relaxation of upwelling circulation on the Northeastern South China Sea shelf. Deep Sea Res. Part II Top. Stud. Oceanogr. 117, 41–52. https://doi.org/10.1016/j.dsr2.2013.12.009.

Gan, J.P., Ho, H.S., Liang, L.L., 2013. Dynamics of intensified downwelling circulation over a widened shelf in the Northeastern South China Sea. J. Phys. Oceanogr. 43 (1), 80–94. https://doi.org/10.1175/jpo-d-12-02.1.

Herrmann, M., Somot, S., Calmanti, S., Dubois, C., Sevault, F., 2011. Representation of spatial and temporal variability of daily wind speed and of intense wind events over the Mediterranean Sea using dynamical downscaling: impact of the regional climate model configuration. Nat. Hazards Earth Syst. Sci. 11 (7), 1983–2001. https://doi.org/10.5194/nhess-11-1983-2011.

Hong, S.-Y., Kim, J.-H., Lim, J.-o., Dudhia, J., 2006a. The WRF single moment microphysics scheme (WSM). Journal of the Korean Meteorological Society 42, 129–151.

Hong, S.Y., Noh, Y., Dudhia, J., 2006b. A new vertical diffusion package with an explicit treatment of entrainment processes. Mon. Weather Rev. 134 (9), 2318–2341. https://doi.org/10.1175/mwr3199.1.

Jiang, L., Xia, M., 2016. Dynamics of the Chesapeake Bay outflow plume: realistic plume simulation and its seasonal and interannual variability. J. Geophys. Res.: Oceans 121, 1424–1445.

Kain, J.S., 2004. The Kain-Fritsch convective parameterization: an update. J. Appl. Meteorol. 43 (1), 170–181. https://doi.org/10.1175/1520-0450(2004)043<0170:Tkcpau>2.0.Co, 2.

Lai, W.F., Gan, J.P., Liu, Y., Liu, Z.Q., Xie, J.P., Zhu, J., 2021. Assimilating in situ and remote sensing observations in a highly variable estuary-shelf model. J. Atmos. Ocean. Technol. 38 (3), 459–479. https://doi.org/10.1175/jtech-d-20-0084.1.

Lai, W.F., Pan, J.Y., Devlin, A.T., 2018. Impact of tides and winds on estuarine circulation in the Pearl River Estuary. Continent. Shelf Res. 168, 68–82. https://doi.org/10.1016/j.csr.2018.09.004.

Langlais, C., Barnier, B., Molines, J.M., Fraunié, P., Jacob, D., Kotlarski, S., 2009. Evaluation of a dynamically downscaled atmospheric reanalyse in the prospect of forcing long term simulations of the ocean circulation in the Gulf of Lions. Ocean Model. 30 (4), 270–286. https://doi.org/10.1016/j.ocemod.2009.07.004.

Larson, M., Bellanca, R., Jönsson, L., Chen, C., Shi, P., 2005. A model of the 3D circulation, salinity distribution, and transport pattern in the Pearl River Estuary, China. J. Coast Res. 215, 896–908. https://doi.org/10.2112/03-105a.1.

Liu, Z., Gan, J., 2016. Open boundary conditions for tidally and subtidally forced circulation in a limited-area coastal model using the Regional Ocean Modeling System (ROMS). J. Geophys. Res.: Oceans 121 (8), 6184–6203. https://doi.org/10.1002/2016jc011975.

Liu, Z.Q., Gan, J.P., 2014. Modeling study of variable upwelling circulation in the East China Sea: response to a coastal promontory. J. Phys. Oceanogr. 44 (4), 1078–1094. https://doi.org/10.1175/jpo-d-13-0170.1.

Liu, Z.Q., Gan, J.P., 2020. A modeling study of estuarine-shelf circulation using a composite tidal and subtidal open boundary condition. Ocean Model. 147 https://doi.org/10.1016/j.ocemod.2019.101563.

Mellor, G.L., Yamada, T., 1982. Development of a turbulence closure-model for geophysical fluid problems. Rev. Geophys. 20 (4), 851–875.

Michalakes, J., Dudhia, J., Gill, D., Klemp, J., Skamarock, W., 1998. Design of a Next-generation Regional Weather Research and Forecast Model. Towards Teracomputing. World Scientific, River Edge, New Jersey, pp. 117–124.

Mlawer, E.J., Taubman, S.J., Brown, P.D., Iacono, M.J., Clough, S.A., 1997. Radiative transfer for inhomogeneous atmospheres: RRTM, a validated correlated-k model for the longwave. J. Geophys. Res. Atmos. 102 (D14), 16663–16682. https://doi.org/10.1029/97jd00237.

Myksvoll, M.S., Sundby, S., Ådlandsvik, B., Vikebø, F.B., 2011. Retention of coastal cod eggs in a fjord caused by interactions between egg buoyancy and circulation pattern. Marine and Coastal Fisheries 3 (1), 279–294. https://doi.org/10.1080/19425120.2011.595258.

O'Neill, L.W., Chelton, D.B., Esbensen, S.K., 2005. High-resolution satellite measurements of the atmospheric boundary layer response to SST variations along the Agulhas Return Current. J. Clim. 18 (14), 2706–2723. https://doi.org/10.1175/jcli3415.1.

O'Neill, L.W., Chelton, D.B., Esbensen, S.K., 2010. The effects of SST-induced surface wind speed and direction gradients on midlatitude surface vorticity and divergence. J. Clim. 23 (2), 255–281. https://doi.org/10.1175/2009jcli2613.1.

Oerder, V., Colas, F., Echevin, V., Masson, S., Hourdin, C., Jullien, S., Madec, G., Lemarié, F., 2016. Mesoscale SST-wind stress coupling in the Peru-Chile current system: which mechanisms drive its seasonal variability? Clim. Dynam. 47 (7–8), 2309–2330. https://doi.org/10.1007/s00382-015-2965-7.

Oerder, V., Colas, F., Echevin, V., Masson, S., Lemarie, F., 2018. Impacts of the mesoscale ocean-atmosphere coupling on the Peru-Chile ocean dynamics: the current-induced wind stress modulation. Journal of Geophysical Research-Oceans 123 (2), 812–833. https://doi.org/10.1002/2017jc013294.

Pan, J.Y., Lai, W.F., Devlin, A.T., 2020. Channel-trapped convergence and divergence of lateral velocity in the Pearl River Estuary: influence of along-estuary variations of channel depth and width. Journal of Geophysical Research-Oceans 125 (1). https://doi.org/10.1029/2019jc015369.

Pullen, J., 2003. Coupled ocean-atmosphere nested modeling of the Adriatic Sea during winter and spring 2001. J. Geophys. Res. 108 (C10) https://doi.org/10.1029/2003jc001780.

Pullen, J., Doyle, J.D., Signell, R.P., 2006. Two-way air-sea coupling: a study of the Adriatic. Mon. Weather Rev. 134 (5), 1465–1483. https://doi.org/10.1175/mwr3137.1.

Ricchi, A., Miglietta, M.M., Falco, P.P., Benetazzo, A., Bonaldo, D., Bergamasco, A., Sclavo, M., Carniel, S., 2016. On the use of a coupled ocean-atmosphere-wave model during an extreme cold air outbreak over the Adriatic Sea. Atmos. Res. 172, 48–65. https://doi.org/10.1016/j.atmosres.2015.12.023.

Seo, H., Miller, A.J., Roads, J.O., 2007. The scripps Coupled Ocean-atmosphere regional (SCOAR) model, with applications in the eastern pacific sector. J. Clim. 20 (3), 381–402. https://doi.org/10.1175/jcli4016.1.

Shchepetkin, A.F., McWilliams, J.C., 2005. The regional oceanic modeling system (ROMS): a split-explicit, free-surface, topography-following-coordinate oceanic model. Ocean Model. 9 (4), 347–404. https://doi.org/10.1016/j.ocemod.2004.08.002.

Smolarkiewicz, P.K., 1984. A fully multidimensional positive defnite advection transport algorithm with small implicit diffusion. J. Comput. Phys. 54 (2), 325–362.

Sun, L., Liang, X.Z., Xia, M., 2020. Developing the coupled CWRF-FVCOM modeling system to understand and predict atmosphere-watershed interactions over the great lakes region. J. Adv. Model. Earth Syst. 12, e2020MS002319 https://doi.org/10.1029/2020MS002319.

Warner, J.C., Armstrong, B., He, R.Y., Zambon, J.B., 2010. Development of a Coupled Ocean-Atmosphere-Wave-Sediment transport (COAWST) modeling system. Ocean Model. 35 (3), 230–244. https://doi.org/10.1016/j.ocemod.2010.07.010.

Warner, J.C., Sherwood, C.R., Signell, R.P., Harris, C.K., Arango, H.G., 2008. Development of a three-dimensional, regional, coupled wave, current, and sediment-transport model. Comput. Geosci. 34 (10), 1284–1306. https://doi.org/10.1016/j.cageo.2008.02.012.

Xie, L., Eggleston, D.B., 1999. Computer simulations of wind-induced estuarine circulation patterns and estuary-shelf exchange processes: the potential role of wind forcing on larval transport. Estuar. Coast Shelf Sci. 49 (2), 221–234. https://doi.org/10.1006/ecss.1999.0498.

Zu, T., Gan, J., 2015. A numerical study of coupled estuary-shelf circulation around the Pearl River Estuary during summer: responses to variable winds, tides and river discharge. Deep Sea Res. Part II Top. Stud. Oceanogr. 117, 53–64.

Zu, T., Wang, D., Gan, J., Guan, W., 2014. On the role of wind and tide in generating variability of Pearl River plume during summer in a coupled wide estuary and shelf system. J. Mar. Syst. 136, 65–79.